RSC Advances

PAPER

View Article Online
View Journal | View Issue

Cite this: *RSC Adv.*, 2021, **11**, 20479

Nickel hydroxide as a non-noble metal co-catalyst decorated on $Cd_{0.5}Zn_{0.5}S$ solid solution for enhanced hydrogen evolution

Dan Chen, * Yao Xu, Yingying Zhang, Wenyu Sheng and Guangren Qian

The study of non-noble metal photocatalysts provides practical significance for hydrogen evolution applications. Herein, new $Cd_{0.5}Zn_{0.5}S/Ni(OH)_2$ catalysts were fabricated through simple hydrothermal and precipitation methods. The photocatalytic performance of the $Cd_{0.5}Zn_{0.5}S/Ni(OH)_2$ composites under visible light was significantly improved, which was attributed to the wider visible light absorption range and less recombination of electron–hole pairs. The composite with a $Ni(OH)_2$ content of 10% showed the best hydrogen evolution rate of 46.6 mmol g^{-1} h^{-1}, which was almost 9 times higher than that of pristine $Cd_{0.5}Zn_{0.5}S$. The severe photo-corrosion of $Cd_{0.5}Zn_{0.5}S$ was greatly improved, and the $Cd_{0.5}Zn_{0.5}S/Ni(OH)_2$ composite exhibited a very high hydrogen evolution rate after three repeated tests. The excellent photocatalytic performance was due to the non-noble metal $Ni(OH)_2$ co-catalyst. The excited electrons were transferred to the co-catalyst, which reduced electron–hole recombination. Moreover, the co-catalyst offered more sites for photocatalytic reactions. This study researched the mechanism of a co-catalyst composite, providing new possibilities for non-noble metal photocatalysts.

Received 20th May 2021
Accepted 27th May 2021

DOI: 10.1039/d1ra03938e

rsc.li/rsc-advances

1. Introduction

Energy shortages and environmental pollution have become serious problems plaguing the development of various countries; thus, the search for green energy has aroused widespread concern.[1–4] Hydrogen energy is characterized by low environmental pollution and high energy density,[5–7] and is expected to become a substitute for fossil fuels.[8–12] Since the Honda–Fujishima effect was discovered in 1972,[13] water splitting photocatalytic technology has been considered the most potent method for obtaining hydrogen energy.[14] However, the bandgap of TiO_2 is relatively wide (3.2 eV), and TiO_2 can only respond to ultraviolet light, which occupies 3% to 5% of solar energy.[15,16] Low light availability blocks the further application of photocatalysis. Thus, many new photocatalysts with promising visible light responses have been researched and reported.[17–20]

In the past few years, sulfide has drawn wide attention due to its low price and strong visible light absorption.[21,22] $Cd_{0.5}Zn_{0.5}S$ solid solution, a catalyst coupling CdS and ZnS, has a suitable bandgap width and band edge position, and has seen extensively investigated in the field of photocatalysis.[23,24] However, the fast carrier recombination and severe photo-corrosion of this material have a great adverse influence on photocatalytic activity.[25,26] To date, researchers have tried a variety of methods to address these problems. Xue *et al.* constructed 2D mesoporous ultrathin $Cd_{0.5}Zn_{0.5}S$ nanosheets, and the hydrogen evolution rate was 2.2 times higher than that of $Cd_{0.5}Zn_{0.5}S$ nanoparticles.[27] Zhang *et al.* reported a $NiSe_2/Cd_{0.5}Zn_{0.5}S$ type-II heterojunction whose photocatalytic hydrogen evolution rate was approximately 2.1 times that of pristine $Cd_{0.5}Zn_{0.5}S$.[28] Other works, such as those investigating $Co_2P/Cd_{0.5}Zn_{0.5}S$,[29] ZIF-8/$Cd_{0.5}Zn_{0.5}S$,[30] $Bi_2S_3/Cd_{0.5}Zn_{0.5}S$,[31] and g-$C_3N_4/Cd_{0.5}Zn_{0.5}S$,[32] showed the feasibility of facilitating photogenerated electron migration. However, work on co-catalyst-modified $Cd_{0.5}Zn_{0.5}S$ is relatively lacking.

Currently, nickel hydroxide co-catalyst is widely studied because of its low price, easy synthesis and layered structure.[33–35] Many studies have shown that nickel hydroxide co-catalyst can enhance responsiveness to visible light, and promote the separation of photo-generated electron–hole pairs. Cao *et al.* used an electrostatic method to decorate negatively charged 3D g-C_3N_4 with positively charged 2D $Ni(OH)_2$ nanosheets, and the synthesized composite released approximately 76 times more hydrogen than pristine g-C_3N_4.[36] Liu *et al.* constructed a new 2D/2D layer-like $Ni(OH)_2/Bi_4Ti_3O_{12}$ composite with fast separation of electron–hole pairs due to the interfacial interaction and coupling interfaces.[37] In addition, some studies have revealed that nickel hydroxide co-catalyst can provide reductive active sites. For example, Liu *et al.* prepared $Ni(OH)_2$ with a three-dimensional nano-flower structure, and the special structure inhibited interlamellar superposition, and provided more active sites.[38] Furthermore, Li *et al.* reported that doped Ni^{2+} exhibited a doping energy level, which accelerated the separation of photogenerated electrons, improving the full-spectrum activation.[39] In short, it can be expected that nickel

School of Environmental and Chemical Engineering, Shanghai University, No. 99 Shangda Road, Shanghai 200444, China. E-mail: dchen@shu.edu.cn

hydroxide co-catalyst loaded on $Cd_{0.5}Zn_{0.5}S$ will have excellent photocatalytic performance.

In this study, $Cd_{0.5}Zn_{0.5}S$ solid solution was synthesized by a simple hydrothermal method. Our work explored a new combination of $Ni(OH)_2$ and $Cd_{0.5}Zn_{0.5}S$ in which $Ni(OH)_2$ was decorated as a co-catalyst on $Cd_{0.5}Zn_{0.5}S$ by a chemical deposition method. $Cd_{0.5}Zn_{0.5}S/Ni(OH)_2$ composites with different $Ni(OH)_2$ contents of 5%, 10%, 15%, and 20% were prepared to explore the impact of diverse co-catalyst contents on hydrogen evolution activity. In this system, the modification of $Ni(OH)_2$ greatly improved the photoactivity of pristine $Cd_{0.5}Zn_{0.5}S$, and the electron–hole pairs were effectively separated. The composite was characterized through ultraviolet-visible diffuse reflectance spectroscopy (UV-vis DRS), photoluminescence (PL) spectroscopy, X-ray photoelectron spectroscopy (XPS), *etc.*, and a possible photocatalytic mechanism was proposed. This research is expected to provide new ideas for non-noble metal photocatalysts, reducing the cost of photocatalysts, which is meaningful to the practical application of photocatalytic hydrogen evolution.

2. Experimental sections

All analytical reagents were obtained from Sinopharm Chemical Reagent Co., Ltd.

2.1 Preparation of $Cd_{0.5}Zn_{0.5}S$

First, 5 mmol $Cd(AC)_2 \cdot 2H_2O$ and 5 mmol $Zn(AC)_2 \cdot 2H_2O$ were mixed with 20 ml deionized water. Second, 10 ml of $Na_2S \cdot 9H_2O$ (1.250 g) aqueous solution was added dropwise to the beaker under magnetic stirring. Third, the above-synthesized yellow suspension was transferred to a polytetrafluoroethylene reactor for hydrothermal reaction at a temperature of 200 °C for 12 h. Fourth, the precipitate was centrifuged, washed a few times with deionized water and absolute ethanol and then dried at 60 °C for 12 h. The prepared $Cd_{0.5}Zn_{0.5}S$ catalyst was named CZS.

2.2 Preparation of CZS/Ni

A total of 0.400 g CZS was added to 50 ml 0.25 M NaOH solution and subjected to ultrasonic dispersion for 0.5 h. A total of 3.3 ml, 6.6 ml, 9.9 ml, or 13.2 ml of 0.05 M $Ni(NO_3)_2$ aqueous solution was added dropwise under continuous stirring. Then, the mixture was stirred at ambient temperature for 2 h. After that, the product was washed several times with deionized water and ethanol. Then, the precipitate was dried at 60 °C for 12 h, and named CZS/Ni-5, CZS/Ni-10, CZS/Ni-15, or CZS/Ni-20, respectively.

2.3 Characterizations

X-ray diffraction (XRD, Rigaku Ultimate IV) was carried out to analyse the crystallinity of the materials. The morphology and surface structure were determined by scanning electron microscopy (SEM, SU8010, Hitachi Japan). The microstructure was analysed by transmission electron microscopy (TEM, JEM-2100F). The surface composition and chemical state were recorded on a ThermoFisher ESCALAB 250Xi X-ray photoelectron spectroscopy (XPS) instrument equipped with a monochromatic Al Ka X-ray source ($h\nu = 1486.6$ eV). UV-vis absorption spectroscopy was performed on a UV-vis spectrophotometer (UV-2600, Shimadzu, Japan). The Brunauer–Emmett–Teller (BET) surface area and pore size distribution were tested with an Autosorb-IQ2 automatic specific surface area and pore size distribution analyser (Quantachrome, America). PL analysis was performed using a Gangdong Technology F-320 PL spectrophotometer.

2.4 Photocatalytic experiments

The photoactivity of the above-fabricated materials was examined by an online photocatalytic reaction system (CEL-SPH2N, Beijing), with a 300 W Xe lamp (CEL-SPH2N, Beijing) under visible light illumination ($\lambda \geq 420$ nm). A cooled circulating water system was adopted to keep the reaction at approximately 6 °C. In general, 25 mg and 50 ml of aqueous solutions containing 10 ml lactic acid and 40 ml deionized water were mixed. Before visible light irradiation, the air in the system was evacuated to keep the reaction system under a vacuum state throughout the reaction. A gas chromatograph (GC-7920, China, N_2 as carrier) was employed to analyse the evolution of hydrogen every 0.5 h.

2.5 Photoelectrochemical measurements

The photoelectrochemical experiment was carried out by using an electrochemical workstation (CHI 760E, Shanghai Chenhua Co., Ltd.). To mimic a traditional electrochemical system, the photocatalyst was applied to the surface of the working electrode. Pt foil was used as the counter electrode, and a saturated calomel electrode (SCE) was used as the reference electrode. During all tests, the experimental effective area was 0.8×1 (cm). The preparation process for the working electrode was as follows. First, 10 mg of photocatalyst was mixed with 1 ml deionized water. Then, after adding 50 μl Nafion to the mixture, the sample was sonicated for 30 min to achieve uniform mixing. Finally, 30 μl of the obtained suspension was added dropwise to an indium tin oxide (ITO) glass plate and dried at room temperature. Photocurrent response characterization was conducted by using a 300 W Xe lamp as the light source ($\lambda > 420$ nm). The bias voltage and the illumination time interval were 0 V and 20 s, respectively. The frequency range of electrochemical impedance spectroscopy (EIS) was 0.1–100 kHz.

3. Results and discussion

3.1 Structural analysis

The crystallinity and phase purity of the samples were determined by XRD, as shown in Fig. 1. The XRD pattern of CZS was not a simple superposition of the patterns of CdS and ZnS (JCPDS PDF#05-0566). Compared with the pattern of pristine CdS (JCPDS PDF#06-0314), the XRD peaks of the synthesized composites shifted to higher values, which may be due to the different ionic radii of Cd^{2+} (0.97 Å) and Zn^{2+} (0.74 Å). Hence,

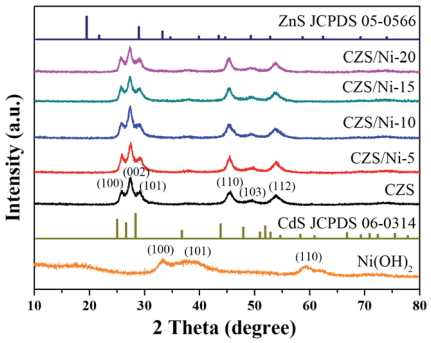

Fig. 1 XRD patterns of pristine CZS and CZS/Ni composites.

the synthesized CZS showed a special solid solution structure, which was consistent with other works.[40–42] The pristine CZS and CZS/Ni composites showed the same XRD patterns, revealing that modified the $Ni(OH)_2$ co-catalyst did not destroy the original structure of CZS. The pristine CZS and CZS/Ni composites showed characteristic peaks at $2\theta = 25.7°$, 27.3°, 29.0°, 45.3°, 49.3° and 53.7°, which were consistent with the (100), (002), (101), (110), (103) and (112) planes, respectively. However, the XRD patterns of the CZS/Ni composites did not exhibit the diffraction peaks of $Ni(OH)_2$ because of the low content of co-catalyst. The existence of $Ni(OH)_2$ in the CZS/Ni composites needed to be further confirmed.

The microscopic morphology of the CZS/Ni-10 composite was observed by SEM, and Fig. 2 shows the results. From Fig. 2a and b, the synthesized composite resembled irregular nanoparticles with a size of approximately 10–50 nm. This result revealed that CZS and $Ni(OH)_2$ were both nanostructure ed. The compositional distribution of the composite was analysed by EDS mapping. The results showed that Cd (Fig. 2d), Zn (Fig. 2e), and S (Fig. 2f) were evenly distributed. In addition, Ni (Fig. 2g) was uniformly dispersed, with a content less than that of CZS, indicating the successful doping of $Ni(OH)_2$. According to Fig. 2c, the content ratio of Cd^{2+} and Zn^{2+} in the CZS/Ni-10 composite was 0.99 : 1, which was close to the theoretical ratio of 1 : 1, further proving that the synthesized CZS was $Cd_{0.5}Zn_{0.5}S$. The results indicated that the $Ni(OH)_2$ co-catalyst had been modified on CZS and the CZS/Ni-10 composite was successfully synthesized.

The synthesis of the composite was further verified by TEM. From Fig. 3a, the $Ni(OH)_2$ co-catalyst was anchored uniformly on the CZS. Exploring the crystal plane (Fig. 3b), we observed lattice fringes at 0.32 nm and 0.26 nm, according to the XRD results and Bragg equation, which were consistent with the (002) plane of CZS and (100) plane of $Ni(OH)_2$, respectively, matching well with the SEM mapping results. These results indicated the successful loading of $Ni(OH)_2$, which further proved the synthesis of the CZS/Ni-10 composite.

The elemental composition and chemical state of the CZS/Ni-10 composite were further analysed by XPS. The Cd 3d spectrum of the composite in Fig. 4b shows peaks at 411.65 and 404.9 eV, matching well with the peaks of Cd $3d_{3/2}$ and Cd $3d_{5/2}$, respectively, indicating the typical binding energy of Cd^{2+}.[31] Similar to the Cd 3d spectrum, the Zn 2p spectrum (Fig. 4c) of the composite with peaks at Zn $2p_{1/2}$ and Zn $2p_{3/2}$ showed the oxidation state of Zn^{2+}. The S 2p spectrum of the composite (Fig. 4d) can be separated into two different peaks at 162.62 and 161.44 eV, which correspond well to S $2p_{1/2}$ and S $2p_{3/2}$. The binding energy difference between the two peaks was limited to 1.2 eV, and the area restriction $p_{(1/2)}/p_{(3/2)} = 1 : 2$, indicating the presence of S2-in the composite. In Fig. 4e, the binding energies at 873.49 and 855.75 eV correspond to the characteristic peaks of Ni $2p_{1/2}$ and Ni $2p_{3/2}$, respectively, with satellite peaks of 879.50 and 861.48 eV, which conform to the standard peaks of nickel hydroxide.[43–45] The results proved the coexistence of CZS and $Ni(OH)_2$ in the CZS/Ni-10 composite, further indicating the successful synthesis of the composite.

Notably, the binding energies of pristine CZS and the CZS/Ni-10 composite were based on the same calibration of C 1s peak, which was 284.6 eV. Compared with the properties of the pristine CZS, the Cd, Zn, and S in the composite maintained the same state, and the binding energies slightly shifted to higher values (approximately 0.4 eV), indicating that more electrons transferred to the $Ni(OH)_2$ co-catalyst through interface interactions.[46,47] The results showed that photogenerated electrons can transfer to the co-catalyst during the photocatalytic process, promoting the separation of hole–electron pairs. In addition, Fig. 4f shows that the valence band (VB) potential of CZS was located at 1.55 eV.

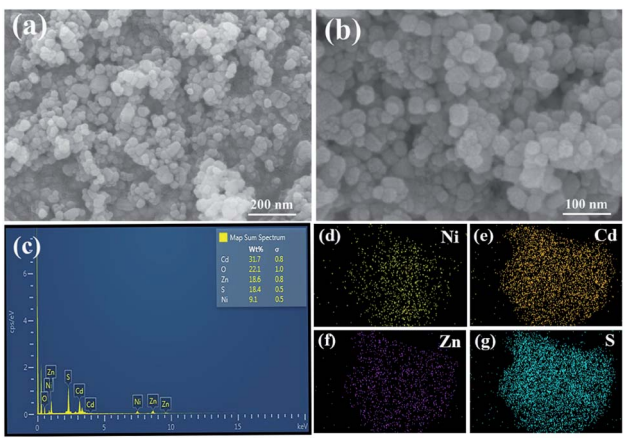

Fig. 2 (a and b) SEM images at different magnifications of the CZS/Ni composites and the corresponding element mapping for (d) Cd, (e) Zn, (f) S and (g) Ni.

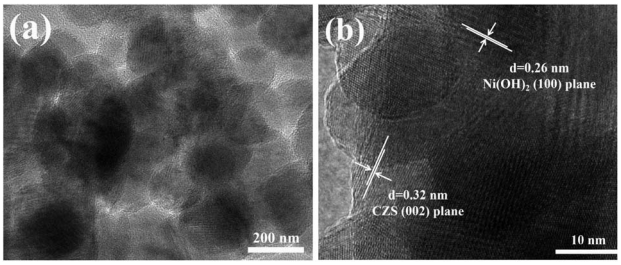

Fig. 3 (a) TEM, and (b) HRTEM images of CZS/Ni-10 composite.

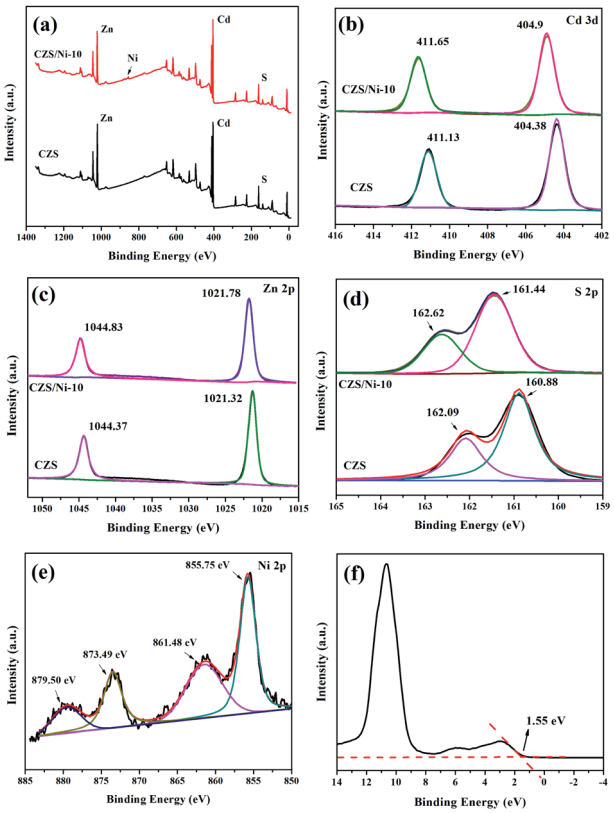

Fig. 4 The XPS spectra of (a) CZS/Ni-10 composite, (b) Cd 3d, (c) Zn 2p, (d) S 2p, (e) Ni 2p, and (f) valence-band.

Fig. 5a shows the UV-Vis DRS spectra of the pristine CZS and CZS/Ni composites. As observed in Fig. 5a, $Ni(OH)_2$ showed light absorptions covering the full spectrum due to the transitions of Ni^{2+} in oxygen octahedral sites,[37,48] and CZS showed an absorption edge of 525 nm. Compared with the results for pristine CZS, the CZS/Ni composites exhibited similar absorption band edges. As shown in Fig. 5b, according to the Kubelka–Munk equation, the band gaps of pristine CZS and the CZS/Ni-10 composite were 2.60 eV and 2.63 eV, respectively. The band gap changed was may be due to band bending at the junction of two semiconductors. In addition, the composites showed additional absorption in the range of 550–800 nm, which corresponded to the absorption of $Ni(OH)_2$. It can be inferred that

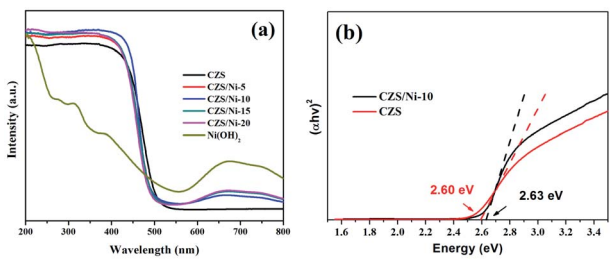

Fig. 5 (a) UV-Vis DRS spectra of pristine CZS and CZS/Ni composites (b) the estimated band gaps of exfoliated pristine CZS and CZS/Ni-10 composites.

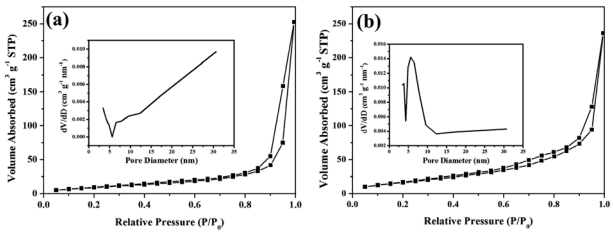

Fig. 6 Nitrogen adsorption–desorption isotherms and corresponding pore size distributions (inset) of (a) pristine CZS and (b) CZS/Ni-10 composite.

$Ni(OH)_2$ was successfully incorporated and the co-catalyst did not destroy the morphology of the original material. Thus, the CZS/Ni composites had a wider visible light absorption range than CZS, which provided more charge carriers for photocatalytic activity, improving hydrogen evolution.

The nitrogen adsorption and desorption isotherms as well as the corresponding pore size distributions of the pristine CZS and CZS/Ni-10 samples are shown in Fig. 6. These absorption–desorption isotherms were classified as type IV,[49] with obvious hysteresis loops at a relative pressure of 0.9–1.0. The shapes of the hysteresis loops are consistent with type H3, indicating the mesoporous structure of the samples. Compared with the results for pristine CZS (Fig. 6a), the hysteresis loop of the CZS/Ni-10 (Fig. 6b) composite was narrower, which could imply that the co-catalyst influenced the pore structure. The pore size distributions (inset) showed pore sizes ranging from 3 to 31 nm, which further proved the existence of mesopores. The presence of mesopores favored multilight scattering/reflection, resulting in enhanced harvesting of the exciting light and thus improved photocatalytic activity.[50,51]

Table 1 demonstrates the BET surface areas, pore volume and pore sizes of the pristine CZS and CZS/Ni-10 composite. The BET surface area of the CZS/Ni-10 composite (68.1 $m^2\ g^{-1}$) was larger than that of pristine CZS (44.1 $m^2\ g^{-1}$), indicating an increased reaction area and therefore providing more active sites.[52] Thus, the photocatalytic performance was improved. Moreover, the average pore size of CZS/Ni-10 was significantly reduced, which may be due to some co-catalyst filling the CZS pores.

3.2 Photocatalytic H_2 evolution performance

The photocatalytic hydrogen evolution performance of the above-synthesized materials was assessed under visible light illumination ($\lambda \geq 420$ nm), with lactic acid (20%) as the sacrificial reagent.

Table 1 BET surface areas and pore volume analysis of pure CZS and CZS/Ni-10 composite

Samples	S_{BET} ($m^2\ g^{-1}$)	Pore volume ($cm^3\ g^{-1}$)	Pore size (nm)
Pristine CZS	44.1	0.25	30.7
CZS/Ni-10	68.1	0.19	5.6

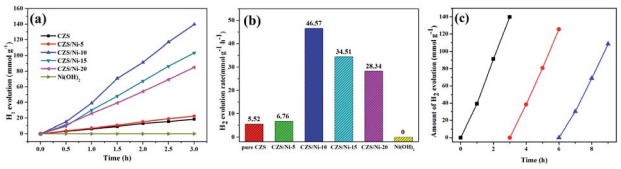

Fig. 7 (a) Photocatalytic H_2 evolution in 3 h, (b) H_2 evolution rate of pristine CZS and CZS/Ni composites, (c) cycling test of photocatalytic H_2 evolution of CZS/Ni-10 composite.

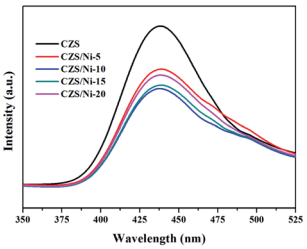

Fig. 8 PL spectra of pristine CZS and CZS/Ni composite.

As observed in Fig. 7a, after 3 h of continuous irradiation, the photo-reactivity of pristine CZS was the poorest, producing only 16.6 mmol hydrogen. At a $Ni(OH)_2$ loading content of 5%, the increase in hydrogen evolution was not obvious. The composite with a loading content of 10% had the best hydrogen evolution performance, reaching 46.57 mmol g^{-1} h^{-1}, which was approximately 8.4 times higher than that of pristine CZS (Fig. 7b). However, with further increases in $Ni(OH)_2$ loading, the photocatalytic activity of the composite decreased dramatically, which might be due to excess co-catalyst covering the active sites of CZS.[53] The above results demonstrated that loading $Ni(OH)_2$ co-catalyst can greatly enhance the photocatalytic activity. The reason may be that the migration and separation rates of charge carriers were improved. It should be noted that the photocatalytic hydrogen evolution rate in this work is substantially higher than other reported works,[54–57] as shown in Table 2.

A three-cycle hydrogen evolution experiment was carried out to verify the reusability of the CZS/Ni-10 composite, and Fig. 7c shows the results. After three cycles, the photocatalytic evolution of the composite was decreased (125 mmol g^{-1} to 108.4 mmol g^{-1}) but was still 6.5 times that of pristine CZS, indicating excellent reusability. Compared with the results of other works on sulfides,[58,59] the stability of the composite was significantly increased, avoiding severe photo-corrosion. The decreased hydrogen evolution can be ascribed to the co-catalyst falling off the support; the same phenomena have been observed in similar composites.[60,61] Subsequent measures can be taken to prevent the co-catalyst from falling off to maintain high photocatalytic activity.

3.3 Charge transfer studies

PL spectroscopy was performed to study the recombination process of photogenerated electron–hole pairs, and Fig. 8 shows the results. The PL intensity of the CZS/Ni composites was lower than that of pristine CZS, which contributed to the interfacial interaction of CZS and $Ni(OH)_2$, promoting the transfer of electrons to the co-catalyst. The results demonstrated that the photogenerated electron–hole pairs of the CZS/Ni-10 composite had the lowest recombination rate, which was consistent with the effect of photocatalytic evolution.

The recombination of charge carriers was identified by transient photocurrent responses (I–t curves). Fig. 9a clearly shows that the photocurrent density of the CZS/Ni-10 composite was higher than that of pristine CZS. It can be inferred that the modification of the co-catalyst enhanced the absorption of visible light, promoting the generation of electrons. Some Ni^{2+} ions dissociated from $Ni(OH)_2$,[62] effectively facilitating the transfer efficiency of photogenerated electrons. In addition, the current density of pristine CZS decreased, indicating severe photo-corrosion. Instead, the CZS/Ni-10 composite retained a stable density, showing excellent resistance to photo-corrosion. EIS Nyquist plots (Fig. 9b) revealed that the arc radius of the CZS/Ni-10 composite was smaller than that of pristine CZS, indicating the higher electron donor density and excellent electrical conductivity of the former,[63] which were beneficial to the transfer of electrons. The photoelectrochemical results coincided with the hydrogen evolution

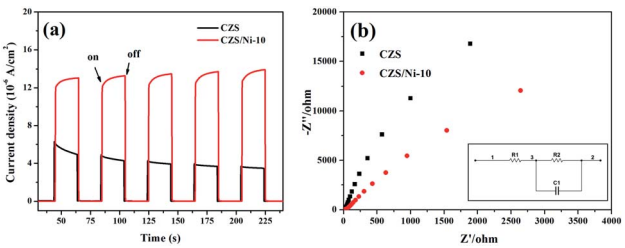

Fig. 9 (a) The transient photocurrent responses (I–t curves) and (b) EIS Nyquist plots of pristine CZS and CZS/Ni-10 composite (inset shows the equivalent circuit).

Table 2 Hydrogen evolution activity of CZS-based photocatalysts

Photocatalyst	Light source	Solution	Activity (mmol h^{-1} g^{-1})	Ref.
$Co_{0.85}Se$ (1.5 wt%)/$Cd_{0.5}Zn_{0.5}S$	300 W Xe lamp ($\lambda \geq 420$ nm)	0.2 M Na_2S and 0.2 M Na_2SO_3	30.37	54
20%-$NiTiO_3$/$Cd_{0.5}Zn_{0.5}S$	300 W Xe lamp ($\lambda \geq 420$ nm)	0.55 M Na_2S and 0.15 M Na_2SO_3	26.45	55
$Cd_{0.5}Zn_{0.5}S$/HNTs-3 wt%	300 W Xe lamp ($\lambda > 400$ nm)	0.1 M Na_2S and 0.1 M Na_2SO_3	25.67	56
13 wt% Fe_2P/$Cd_{0.5}Zn_{0.5}S$	300 W Xe lamp	20 vol% lactic acid	24.84	57

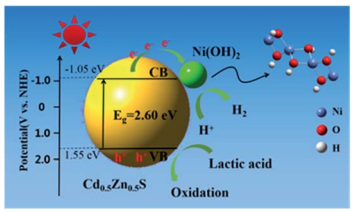

Fig. 10 Proposed mechanism of CZS/Ni-10 composite for photocatalytic H_2 evolution under visible light irradiation.

results, which indicated that $Ni(OH)_2$ can accelerate the transfer of electrons and reduce the recombination of electron–hole pairs, thereby improving the photocatalytic activity.

3.4 Photocatalytic mechanism

The mechanism of the CZS/Ni-10 composite was proposed as follows. First, the VB potential of CZS was identified at 1.55 eV according to the XPS spectrum. From the formula $E_g = E_{VB} - E_{CB}$, the CB potential of CZS was −1.05 eV. According to the previous analysis, the CZS/Ni-10 composite had a wider visible light absorption range and larger surface area, which were beneficial to the generation of photogenerated charge. As seen from Fig. 10, when excited by visible light, electrons transfer to the conduction band (CB). Because the positive potential of Ni^{2+}/Ni^0 (−0.23 V *vs.* NHE, pH = 0) is less negative than that of CZS,[64] photogenerated electrons were transferred to $Ni(OH)_2$ and reduced some Ni^{2+} to Ni^0 atoms, finally forming Ni atoms or clusters. These Ni atoms or clusters further promoted the transfer of electrons to $Ni(OH)_2$, and H^+ was reduced to produce hydrogen.[65] Lactic acid was ionized in the solution, and the positively charged holes on VB were trapped by the negatively charged lactate, which inhibited the oxidation of S^{2-} to S^0. The stability and reusability of the CZS/Ni-10 composite significantly increased, avoiding severe photo-corrosion. In short, the modification of CZS with $Ni(OH)_2$ altered the pathway of electrons, which realized the effective separation of photogenerated electron–hole pairs, improving the effect of photocatalytic hydrogen evolution.

4. Conclusions

In this study, a series of new CZS/Ni composites were synthesized through simple hydrothermal and precipitation methods. The results showed that $Ni(OH)_2$ as a co-catalyst can effectively facilitate the migration of photogenerated h^+ and e^-, provide more reaction sites, and increase the absorption of visible light without changing the original structure of the CZS solid solution. CZS/Ni-10 had the best photocatalytic hydrogen evolution performance (46.6 mmol g^{-1} h^{-1}), which was 8.4 times that of pristine CZS. In addition, the new composite had excellent recyclability and still showed excellent photocatalytic performance after three cycles. The composite had a good photocatalytic hydrogen evolution effect with low cost, which offers far-reaching significance for the study of non-noble metal photocatalysts.

Author contributions

Dan Chen contributed to the conception of the study; Yao Xu performed the experiment and the data analyses and wrote the manuscript; Guangren Qian contributed significantly to analysis and manuscript preparation; Yingying Zhang, Wenyu Sheng helped perform the analysis with constructive discussions.

Conflicts of interest

There are no conflicts to declare.

Acknowledgements

This research work was supported by the National Nature Science Foundation of China (No. 51274138), the Program for Innovative Research Teams in University (No. IRT13078) and the Innovation Program of Shanghai Municipal Education Commission (14YZ014).

Notes and references

1 H. Che, C. Liu, G. Che, G. Liao, H. Dong, C. Li, N. Song and C. Li, *Nano Energy*, 2020, **67**, 104273.
2 L. Lu, S. Zou and B. Fang, *ACS Catal.*, 2021, **11**, 6020–6058.
3 J. Liu, G. Chen and J. Sun, *ACS Appl. Nano Mater.*, 2020, **3**, 11017–11024.
4 S. Yu, S. Song, R. Li and B. Fang, *Nanoscale*, 2020, **12**, 19536–19556.
5 Y. Liu, S. Shen, Z. Li, D. Ma, G. Xu and B. Fang, *Mater. Charact.*, 2021, **174**, 111031.
6 S. Z. Baykara, *Int. J. Hydrogen Energy*, 2018, **43**, 10605–10614.
7 B. Fang, M. Kim, J. H. Kim and J.-S. Yu, *Langmuir*, 2008, **24**, 12068–12072.
8 C. Li, H. Wu, Y. Du, S. Xi, H. Dong, S. Wang and Y. Wang, *ACS Sustainable Chem. Eng.*, 2020, **8**, 12934–12943.
9 B. Fang, J. H. Kim, M.-S. Kim and J.-S. Yu, *Acc. Chem. Res.*, 2013, **46**, 1397–1406.
10 D. Zhang, W. Cao, B. Mao, Y. Liu, F. Li, W. Dong, T. Jiang, Y.-C. Yong and W. Shi, *Ind. Eng. Chem. Res.*, 2020, **59**, 16249–16257.
11 Y. Xing, B. Fang, A. Bonakdarpour, S. Zhang and D. P. Wilkinson, *Int. J. Hydrogen Energy*, 2014, **39**, 7859–7867.
12 G. Liao, J. Fang, Q. Li, S. Li, Z. Xu and B. Fang, *Nanoscale*, 2019, **11**, 7062–7096.
13 A. Fujishima and K. Honda, *Nature*, 1972, **238**, 37–38.
14 G. Liao, C. Li, X. Li and B. Fang, *Cell Rep. Phys. Sci.*, 2021, **2**, 100355.
15 F. Yi, J. Ma, C. Lin, L. Wang, H. Zhang, Y. Qian and K. Zhang, *J. Alloys Compd.*, 2020, **821**, 153557.
16 J. Feng, X. Zhang, G. Zhang, J. Li, W. Song and Z. Xu, *Chemosphere*, 2021, **274**, 129689.
17 R. K. Chava, J. Y. Do and M. Kang, *Appl. Surf. Sci.*, 2018, **433**, 240–248.

18 G. Zhou, M.-F. Wu, Q.-J. Xing, F. Li, H. Liu, X.-B. Luo, J.-P. Zou, J.-M. Luo and A.-Q. Zhang, *Appl. Catal., B*, 2018, **220**, 607–614.
19 Y. Tan, Z. Shu, J. Zhou, T. Li, W. Wang and Z. Zhao, *Appl. Catal., B*, 2018, **230**, 260–268.
20 J.-Z. Cheng, L.-L. Liu, G. Liao, Z.-Q. Shen, Z.-R. Tan, Y.-Q. Xing, X.-X. Li, K. Yang, L. Chen and S.-Y. Liu, *J. Mater. Chem. A*, 2020, **8**, 5890–5899.
21 G. Liao, Y. Gong, L. Zhang, H. Gao, G.-J. Yang and B. Fang, *Energy Environ. Sci.*, 2019, **12**, 2080–2147.
22 M. Zhou, L. Li, S. Zhang, J. Yi, Y. Song, H. Li and H. Xu, *Phys. Status Solidi A*, 2021, **218**, 2100012.
23 F. Liu, F. Xue, Y. Si, G. Chen, X. Guan, K. Lu and M. Liu, *ACS Appl. Nano Mater.*, 2021, **4**, 759–768.
24 K. Khan, X. Tao, M. Shi, B. Zeng, Z. Feng, C. Li and R. Li, *Adv. Funct. Mater.*, 2020, **30**, 2003731.
25 S. Siwatch, V. S. Kundu, A. Kumar, S. Kumar and M. Kumari, *Mater. Res. Express*, 2019, **6**, 085029.
26 C. Zeng, Y. Hu, T. Zhang, F. Dong, Y. Zhang and H. Huang, *J. Mater. Chem. A*, 2018, **6**, 16932–16942.
27 W. Xue, W. Chang, X. Hu, J. Fan and E. Liu, *Chin. J. Catal.*, 2021, **42**, 152–163.
28 X. Zhang, Z. Cheng, P. Deng, L. Zhang and Y. Hou, *Int. J. Hydrogen Energy*, 2021, **46**, 15389–15397.
29 Z. Liang and X. Dong, *J. Photochem. Photobiol., A*, 2021, **407**, 113081.
30 J. Qiu, X.-F. Zhang, X. Zhang, Y. Feng, Y. Li, L. Yang, H. Lu and J. Yao, *J. Hazard. Mater.*, 2018, **349**, 234–241.
31 M. Li, J. Sun, B. Cong, S. Yao and G. Chen, *Chem. Eng. J.*, 2021, **415**, 128868.
32 W. Xue, X. Hu, E. Liu and J. Fan, *Appl. Surf. Sci.*, 2018, **447**, 783–794.
33 L. Dai, Z.-N. Chen, L. Li, P. Yin, Z. Liu and H. Zhang, *Adv. Mater.*, 2020, **32**, 1906915.
34 L. Sha, K. Ye, J. Yin, K. Zhu, K. Cheng, J. Yan, G. Wang and D. Cao, *Chem. Eng. J.*, 2020, **381**, 122603.
35 T. Kou, S. Wang, J. L. Hauser, M. Chen, S. R. J. Oliver, Y. Ye, J. Guo and Y. Li, *ACS Energy Lett.*, 2019, **4**, 622–628.
36 R. Cao, H. Yang, S. Zhang and X. Xu, *Appl. Catal., B*, 2019, **258**, 117997.
37 X. Liu, Z. Zhou, D. Han, T. Wang, C. Ma, P. Huo and Y. Yan, *J. Alloys Compd.*, 2020, **816**, 152530.
38 Y. Liu, J. Xu, Z. Ding, M. Mao and L. Li, *Chem. Phys. Lett.*, 2021, **766**, 138337.
39 J. Li, J. Wang, G. Zhang, Y. Li and K. Wang, *Appl. Catal., B*, 2018, **234**, 167–177.
40 T. Yu, Y. Si, Z. Lv, K. Wang, Q. Zhang, X. Liu, G. Wang, G. Xie and L. Jiang, *Int. J. Hydrogen Energy*, 2019, **44**, 31832–31840.
41 S. Peng, Y. Yang, J. Tan, C. Gan and Y. Li, *Appl. Surf. Sci.*, 2018, **447**, 822–828.
42 L. Ye, C. Han, Z. Ma, Y. Leng, J. Li, X. Ji, D. Bi, H. Xie and Z. Huang, *Chem. Eng. J.*, 2017, **307**, 311–318.
43 Z. Zhang, Q. Yin, L. Xu, J. Zhai, C. Guo, Y. Niu, L. Zhang, M. Li, H. Wang, L. Guan, R. Zhang and H. Lu, *J. Alloys Compd.*, 2020, **816**, 152654.
44 D. Qin, Y. Xia, Q. Li, C. Yang, Y. Qin and K. Lv, *J. Mater. Sci. Technol.*, 2020, **56**, 206–215.
45 C. Kong, F. Zhang, X. Sun, C. Kai and W. Cai, *Inorg. Chem. Commun.*, 2020, **122**, 108264.
46 H. Sun, W. Xue, J. Fan, E. Liu and Q. Yu, *J. Alloys Compd.*, 2021, **854**, 156951.
47 X. Guo, J. Cao, M. Guo, H. Lin, Y. Chen and S. Chen, *Catal. Commun.*, 2019, **119**, 176–179.
48 R. Zhang, T. Ran, Y. Cao, L. Ye, F. Dong, Q. Zhang, L. Yuan and Y. Zhou, *Chem. Eng. J.*, 2020, **382**, 123029.
49 K. S. W. Sing, *Pure Appl. Chem.*, 1985, **57**, 603–619.
50 B. Fang, Y. Xing, A. Bonakdarpour, S. Zhang and D. P. Wilkinson, *ACS Sustainable Chem. Eng.*, 2015, **3**, 2381–2388.
51 B. Fang, A. Bonakdarpour, K. Reilly, Y. Xing, F. Taghipour and D. P. Wilkinson, *ACS Appl. Mater. Interfaces*, 2014, **6**, 15488–15498.
52 F. Yi, H. Gan, H. Jin, W. Zhao, K. Zhang, H. Jin, H. Zhang, Y. Qian and J. Ma, *Sep. Purif. Technol.*, 2020, **233**, 115997.
53 J. Fu, B. Zhu, W. You, M. Jaroniec and J. Yu, *Appl. Catal., B*, 2018, **220**, 148–160.
54 X. Sun and H. Du, *ACS Sustainable Chem. Eng.*, 2019, **7**, 16320–16328.
55 B. Li, W. Wang, J. Zhao, Z. Wang, B. Su, Y. Hou, Z. Ding, W.-J. Ong and S. Wang, *J. Mater. Chem. A*, 2021, **9**, 10270–10276.
56 S. Lin, Y. Zhang, Y. You, C. Zeng, X. Xiao, T. Ma and H. Huang, *Adv. Funct. Mater.*, 2019, **29**, 1903825.
57 Z. Liang and X. Dong, *J. Colloid Interface Sci.*, 2021, **583**, 196–203.
58 J. Sun, M. Yin, Y. Li, K. Liang, Y. Fan and Z. Li, *J. Alloys Compd.*, 2021, **874**, 159930.
59 P. Zhao and K. Huang, *Cryst. Growth Des.*, 2008, **8**, 717–722.
60 S. Ma, Y. Deng, J. Xie, K. He, W. Liu, X. Chen and X. Li, *Appl. Catal., B*, 2018, **227**, 218–228.
61 X. Zong, J. Han, G. Ma, H. Yan, G. Wu and C. Li, *J. Phys. Chem. C*, 2011, **115**, 12202–12208.
62 J. Zhang, C. Cheng, F. Xing, C. Chen and C. Huang, *Chem. Eng. J.*, 2021, **414**, 129157.
63 J. Shi, S. Li, F. Wang, L. Gao, Y. Li, X. Zhang and J. Lu, *J. Alloys Compd.*, 2018, **769**, 611–619.
64 L. Wang, K. Chen, Z. Gao and Q. Wang, *Appl. Surf. Sci.*, 2020, **529**, 147217.
65 J. Ran, J. Yu and M. Jaroniec, *Green Chem.*, 2011, **13**, 2708–2713.